Title

Hydro-mechanical behavior of heated bentonite buffer for geologic disposal of high-level radioactive waste: A bench-scale X-ray computed tomography investigation

Authors

Chang, Chun
Borglin, Sharon
Chou, Chunwei
et al.

Publication Date

2023-02-01

DOI

10.1016/j.clay.2022.106792

Hydro-mechanical Behavior of Heated Bentonite Buffer for Geologic Disposal of High-Level Radioactive Waste: A Bench-Scale X-ray Computed Tomography Investigation

Chun Chang[1,*], Sharon Borglin[1], Chunwei Chou[1], LianGe Zheng[1], Yuxin Wu[1], Timothy J. Kneafsey[1], Seiji Nakagawa[1], Jens T. Birkholzer[1], Marco Voltolini[2]

1. Energy Geosciences Division, Lawrence Berkeley National Laboratory, Berkeley, CA 94720, USA.
2. Department of Earth Sciences “Ardito Desio”, University of Milan, 20133 Milano, Italy.

[*]Corresponding author. *E-mail address*: chunchang@lbl.gov

Highlights

- Column tests were conducted to investigate bentonite hydration up to 200 ℃
- X-ray CT images revealed strongly dynamic and coupled THMC processes
- Heating induced large density variations and displacements in bentonite backfill
- Mineral precipitation occurred on the canister as a result of coupled THMC processes

Abstract. The behavior of heated bentonite buffer is critical for the security and long-term performance of a geological repository for high-level radioactive waste (HLW). While laboratory column experiments have been conducted to investigate compacted bentonite and coupled THMC (thermal-hydro-mechanical and chemical) processes for a moderate temperature range of up to 100ºC, data for a higher temperature range are limited. Understanding bentonite behavior and coupled THMC processes under higher temperatures (e.g., up to 200ºC) could allow for a more economic repository design and would expand the data and knowledge base for more reliable modeling. In this study, a bench-scale experiment was conducted in a compacted bentonite column experiencing both heating up to 200ºC in the center and hydration from a sand-clay boundary surrounding the column. During the experiment run for 1.5 years, frequent X-ray computed tomography (CT) scanning of bentonite provided insights into the spatiotemporal evolution of (1) hydration/dehydration, (2) clay swelling/shrinkage, (3) displacement, and (4) mineral precipitation. After the experiment, a comprehensive post-dismantling characterization of bentonite samples was conducted. Results showed that the bentonite hydration was axi-symmetrical despite the initial heterogeneity due to packing, confirming the ability of bentonite to seal fast flow/transport paths. Compared to a non-heated control experiment, the heated column showed greater CT density variations along the radial distance, indicating that homogenization of bentonite might be more difficult if a temperature gradient is maintained in the repository. Precipitation of an anhydrite layer occurred in the inner hot zone, pointing to potential concerns about salt precipitation causing canister corrosion. Ultimately, the experiments provided a high-resolution window into the strongly dynamic and coupled behavior of bentonite exposed to heating, hydration and swelling, which will be valuable for improving modeling of coupled processes, especially for the early state of a HLW repository.

Keywords: High-level radioactive waste repository**,** Engineered barrier, Compacted bentonite, X-ray CT imaging, Hydro-mechanical behavior, Coupled THMC processes

1. Introduction

Geologic disposal of high-level radioactive waste (HLW) relies on both natural barriers formed by rock formations and an Engineered Barrier Systems (EBS) in isolating the waste from biosphere (IAEA, 2003). In most repository designs, emplacement tunnels will be backfilled with bentonite material as an engineered barrier element that provides mechanical buffering for the waste canisters, additional retention capacity, and thermal stability (Meunier et al., 1998; Bourg et al., 2003; Sellin and Leupin, 2013). After waste emplacement, the bentonite buffer can be simultaneously heated from the decaying radioactive waste and hydrated from the surrounding host rock (IAEA, 2003), triggering complex coupled THMC (thermal-hydro-mechanical-chemical) processes. These include (1) moisture transport affected by strong capillary forces at the bentonite-rock interface and the large thermal gradient near the heat source; (2) swelling and shrinkage due to bentonite hydration or de-hydration; (3) dilution/concentration, evaporation, migration and exchange of ions impacted by moisture/thermal interactions, (4) dissolution/precipitation and mineral phase transformation, etc. (Zheng et al., 2020). These coupled processes evolve temporally and spatially and lead to changes in bentonite properties (e.g., porosity, permeability), which may be important for short-term barrier system evolution as well as long-term performance (Zheng et al., 2021). Assessing the safety of radioactive waste disposal thus requires a comprehensive understanding of bentonite behavior under geologic disposal conditions.

Extensive field and laboratory experiments have been conducted to investigate the bentonite behavior subject to heating and hydration under conditions relevant to nuclear waste disposal (e.g., Börgesson et al., 2001; ENRESA, 2006; Åkesson et al., 2009; Gómez-

Espina and Villar, 2010; Fernández and Villar, 2010; Rawat et al., 2019; Villar et al., 2018, 2020). For example, the FEBEX (Full-scale Engineered Barrier Experiment in crystalline host rock) project had two large-scale tests: the *in-situ* field test at the Grimsel Test Site (Switzerland) and the mock-up test at CIEMAT (Research Centre for Energy, Environment and Technology) facilities in Madrid (Spain) (Alonso and Ledesma, 2005; ENRESA, 2006). Both of the tests were conducted with maximum bentonite temperatures of 100 °C. Concomitantly, laboratory column tests (ENRESA, 2006; Zheng et al., 2010) were conducted with the heater temperature of 100°C. While long-term (10-20 years) field tests are the ultimate measure to study bentonite buffer at a scale similar to the "real" repository, laboratory column tests can be used to (1) characterize bentonite under a range of conditions and provide useful parameters for models, (2) study TH, THM, THC or THMC evolutions of bentonite in shorter time periods (0.5-3 years) at smaller scales, and (3) support and supplement field tests. For example, in a cylindrical cell, Villar et al. (2008) conducted a long-term (up to 8 year) laboratory tests on compacted bentonite barrier at a heater temperature of 100°C. Bentonite was heated at the bottom surface and hydrated through the top with granitic water. A fully coupled thermo-hydro-mechanical (THM) formulation was developed as a general framework to analyze the experiments. The geochemical behavior of bentonite in the column test was investigated by Fernández and Villar (2010). They observed the increase of pore water salinity and precipitation of calcite and anhydrite due to water evaporation in the heating zone. Villar et al. (2012) further summarized laboratory and field tests on the saturation of compacted bentonite under repository conditions at different scales. Results showed the heterogeneity of bentonite after full saturation in terms of dry density and water content distributions. Common to all the field and laboratory studies described above is that they targeted at a maximum temperature range of about 100°C, which is consistent with the bentonite temperature limit considered in many disposal concepts throughout the world (Hicks et al., 2009).

Some disposal programs have recently started investigating if bentonite barriers can withstand temperatures higher than this 100°C threshold. Higher disposal temperatures would allow for less spacing between heat-emanating waste packages, which in turn would reduce the repository footprint for a given waste volume, allowing for significant cost reductions. Because of this emerging interest, some laboratory and field tests were recently conducted at temperatures higher than 100 °C. For example, the LOT test series at the Äspö Hard Rock Laboratory (HRL) were conducted under temperatures up to 140°C, focusing on identifying and quantifying potential mineralogical alterations in the bentonite exposed to typical repository-like conditions. The overarching conclusion was that the observed mineralogical alterations, as a consequence of the water saturation process and the exposure to high temperature, were relatively small and that these alterations did not change the physical properties to such an extent that the buffer function was jeopardized (Karnland et al., 2009). At the Mont Terri rock laboratory, two column tests were conducted with a heater temperature of 140°C using MX-80 bentonite and a sand-bentonite mixture to support the HE-E heater test (Villar et al., 2012, 2014; Ballarini et al., 2017; Bossart et al., 2017) A series of hydrothermal laboratory tests was conducted to study the geochemical alteration of bentonite, and its interaction with clay rock, granite and concrete, at temperatures up to 300°C (Cheshire et al, 2014; 2018). Both studies did not report significant changes in safety-relevant properties of the bentonite. This is consistent with modeling results from Zheng et al. (2015, 2017), which suggested that bentonite may withstand temperatures up to 200 °C without compromising the buffer's performance. Pusch et al. (2010), however, pointed out that at temperature >100°C, crystalline or amorphous SiO_2 can precipitate and cement the stacks of montmorillonite together and reduce their expandability. This cementation then will compromise the function of EBS by reducing bentonite plasticity and capability to swell under hydration. Vomvoris et al. (2015) also recognized potential temperature-driven physico-chemical processes (cementation, illitization) that could detrimentally affect the bentonite properties at 150 to 200°C. The European project EURAD includes a work package devoted to the "Influence of Temperature on Clay-based Material Behaviour" (HITEC), which evaluates whether or not elevated temperature limits (of 100-150°C) are feasible for a variety of geological disposal concepts, and aims to determine where the buffer safety functions start to be unacceptably impaired (https://www.ejp-eurad.eu/implementation/influence-temperature-clay-based-material-behaviour-hitec). Despite this rising interest, questions remain whether bentonite can sustain its favorable features with temperatures up to 200 °C.

Large uncertainties in laboratory characterizations of bentonite behavior have been recognized (Birkholzer, 2018). For instance, in laboratory column tests, monitoring of bentonite behavior relies on sensors emplaced in the bentonite column (e.g., temperature and relative humidity sensors) or on the test vessel shell (e.g., the stress sensors). The limited 'point' measurements generally lumped over the entire column, however, often involved uncertainties in data interpretation due to the lack of resolutions to capture the spatiotemporal heterogeneity in bentonite behaviors (e.g., Ballarini et al., 2017). A better understanding of bentonite barriers requires improved monitoring resolution to reduce uncertainties in data interpretation, along with well-calibrated parameters. Recent development in X-ray imaging and analysis techniques provided promising approaches for in-situ sample characterizations (e.g., Harjupatana et al., 2015; 2022). Laboratory bench-scale column tests facilitated with frequent high-resolution X-ray CT scanning is expected to be an efficient approach to directly image bentonite and understand its behavior at the repository relevant conditions.

In this study, bench-scale experiments were conducted in a compacted bentonite column experiencing both high temperature heating (up to 200ºC) in the center and hydration from a sand-clay boundary surrounding the column. These experiments fill an important research gap since the existing hydrothermal laboratory tests did not explore the full complexity of coupled THMC processes and bentonite behavior experienced in a repository for high-level radioactive waste disposal. *In-situ* field and laboratory column experiments, on the other hand, have not tested the full temperature regime of up to 200°C. More importantly, a new monitoring methodology—frequent X-ray computed tomography (CT) scanning—was used to provide “real time” spatial information of the HM behavior of bentonite. A control column undergoing only hydration was used for comparison. A comprehensive monitoring approach was applied to investigate bentonite behavior and coupled THMC processes, including (1) the above-mentioned frequent X-ray CT scanning to gain a detailed understanding of bentonite at a sub-millimeter spatial resolution; (2) emplaced sensors providing point measurements, and (3) detailed post-dismantling characterizations of bentonite samples after the experiments.

2. Materials and methods

2.1 Materials

The bentonite used for the experiments was MX-80 Wyoming bentonite (Cetco, IL), which came with granular particles of low moisture (<10%). The raw bentonite material was composed mainly by montmorillonite (79%) from X-ray powder diffraction (XRPD) analysis, similar to Villar (2005) and Karnland et al. (2006). It also contained quartz (9 %), Plagioclase (6%), cristobalite (4%), k-feldspars (1%) and calcite (1%). The CEC was reported at 74 -77 meq/100g, and the major exchangeable cations were: Na (55-61 meq/100g), Ca (10-13 meq/100g) and Mg (3-5 meq/100g) (Villar, 2005; Karnland et al., 2006).

The saturating fluid used for bentonite hydration was made based on the computed MX-80 bentonite pore water chemistry for a closed system under room temperature (Bradbury and Baeyens, 2003). It was a solution dominated by Na^+ and SO_4^{2-} ions with an ionic strength of 0.314 M. Detailed chemical composition of the synthetic solution is presented in Table S1.

2.2 Experimental setup and procedures

An aluminum vessel was designed based on the testing temperature and pressure, and the ability to accommodate cross-sample characterization methods, i.e., X-ray CT imaging and electrical resistivity tomography (ERT) (Figure 1). The inner diameter (ID) of the vessel is 0.17 m, the outer diameter (OD) is 0.19 m, and the length is 0.46 m. A cartridge heater (0.30 m long and 0.006 m OD) was housed in a 0.01 m OD titanium shaft penetrating through the center of the vessel. The end caps for the vessel were also made of aluminum, with multiple electrical and fluid feedthroughs. Eight thermocouple sensors were emplaced at different distances from the heater shaft for heating control and monitoring temperature distributions in the column. Two ERT electrode arrays were emplaced oppositely along the exterior surface of the bentonite column, in contact with the surrounding sand layer. To accommodate the ERT monitoring needs, the internal surface of the vessel, the end caps and other internal components of the vessel were coated with silicone to provide electrical insulation.

A special procedure was developed for moisturizing and packing of the experimental clay column with various sensors precisely installed at the desired locations. The raw material was first sieved to remove large clumps and provide a homogenous sample for the tests. Mesh screen openings at 1000 μm and 600 μm were used, and particles >600 μm were rejected, accounting for 0.75% of the raw material. Microscope images (Figure S1 of the Supporting Information (SI), which could be found online) of the rejected particles showed that they were large clumps of the material same to the sieved fine particles. The sieved bentonite was then mixed with water by spraying to reach final gravimetric water contents of 0.17 and 0.18 (Table 1). Using a customized supporting mold, the moisturized bentonite was compacted in layers with sensors added at pre-defined locations during the process. After packing, the column was frozen to -20 °C, and the supporting mold was then removed so that the bentonite column could stand atop the bottom end cap. The bulk density for the non-heated and heated column was 1.44, 1.41 g/cm^3, respectively. The aluminum pressure vessel was then lowered around the compacted bentonite column, and Accusand quartz sand (Unimin Corporation, Le Sueur, MN) at 1.0 mm grain size was placed between bentonite and the vessel wall. In this way, a high-permeability 0.006 m thick sand layer was created providing a homogeneous hydration boundary along the circumferential surface of the bentonite. The top end cap was the final piece installed before conducting the pre-experiment characterization by X-ray CT scanning and temperature data acquisitions.

Table 1. Summary of the initial and stable conditions of compacted bentonite, column dimensions and hydration conditions for the non-heated and heated columns

	Initial conditions		**Stable conditions by the end of the experiments**	
	Non-heated column	**Heated column**	**Non-heated column**	**Heated column**
Dry density (g/cm^3)	1.20	1.20	1.13[c]	1.14[c]
Bulk density (g/cm^3)	1.46[a]/1.44[b]	1.44[a]/1.41[b]	1.68[a]	1.64[a]
Gravimetric water content	0.17	0.18	0.47[c]	0.46[c]
Porosity	0.53	0.54	0.57[c]	0.57[c]

Column dimensions		**Hydration conditions**	
Length (m)	0.46	Pressure (MPa)	0.83
Inner diameter (m)	0.17	Flow rate (mL/min)	0.11

[a] represents values estimated from X-ray CT scans, [b] represents the gravimetrically measured values. [c] refers to the measurements from collected bentonite samples after dismantling of both columns.

Synthetic solution was first injected into the vessel at a high flow rate via a syringe pump (ISCO 500D, Teledyne) to displace air in the sand layer. Then a back-pressure pump (ISCO 500D, Teledyne) was connected to the outlet of the column. As the solution injection continued, the pressures in the column and the injection and back-pressure pumps increased. When the target pressure was achieved at 0.83 MPa, the back pressure pump was adjusted to constant pressure mode at 0.83 MPa, while the solution injection rate was reduced to 0.11 mL/min. Two tubes were installed in the end caps, one for inlet and one for outlet. These tubes hydraulically connected the annular sand layer with water pumps through the end caps (see Figure 1). Because of the high permeability of the loosely packed sand layer, injected solution can be evenly distributed over the sand surfaces and the stable differential pressure along the vessel monitored by pressure transducers at the inlet and outlet kept <0.02 MPa. Meanwhile, effluent solution was collected for chemical composition analysis. In the heated column, the sand layer was saturated with the synthetic solution at t=1 day and kept constant flow rate at 0.11 mL/min under 0.83 MPa. At t=2 days, the heater was turned on and the temperature of bentonite on the heater shaft was maintained constant at 200°C after 8 days. During the experiment, frequent X-ray CT scanning was conducted for over 1.5 years until both columns were dismantled.

XRPD analysis was also used to characterize the mineralogical changes in bentonite samples after column tests. The instrument employed was a Rigaku SmartLab working in a theta-theta Bragg-Brentano configuration, equipped with a spinning sample holder, employed to improve the data collection statistics, and a D/teX Si strip linear detector. Filtered Cu Kα radiation was used, and an interval between 3° and 68° of 2θ was measured. The data were then analyzed via the Rietveld method using the MAUD software (Lutterotti, 2010). All the samples from the vessels were collected and immediately sealed to prevent moisture loss, and testing processes were designed to minimize loss of moisture during the measurements.

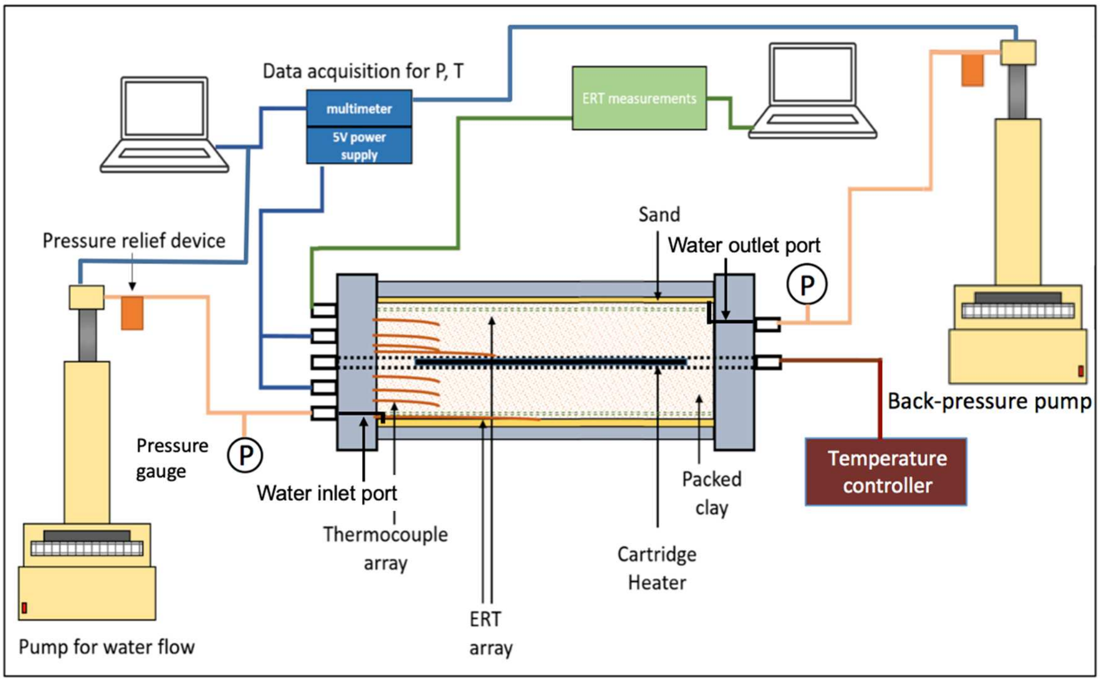

Figure 1. Schematic of the experimental setup.

2.3 X-ray CT imaging and CT density calibration

During the experiment, X-ray CT images provided a 3-D visualization of the CT density distribution, resulting from changes in degree of saturation, clay swelling or structural deformation. A GE Lightspeed 16 medical CT scanner was used to scan the vessels periodically throughout the experiment. Each CT scan was performed at 120 kV and 160 mA, at a voxel size of $400 \times 400 \times 625$ μm^3. It should be noted that the bulk density is dependent on both dry density and water content, i.e., the value increases with increasing water content and dry density. The image processing and analysis were conducted using ImageJ – a public domain JAVA-based software (Rasband, 1997-2022).

The correlation between bentonite bulk density and CT number, i.e., the calibration curve and equation, was obtained by scanning separate columns compacted with bentonite of known bulk densities (see Figure S2 in SI). Note that CT numbers at 0 and 1 g/cm^3 were obtained by scanning air and water, respectively. This close correlation between material bulk density and CT number has been suggested by Mull (1984). To further verify the calibration curve specifically for the experiment, seven bentonite samples were collected in the heated column after dismantling using tube samplers at an internal diameter of 0.7 cm. The bulk wet mass was measured right after sampling. High-resolution X-ray CT scanning was then applied to obtain the sample volume, so that the bulk wet density can be calculated precisely and compared with CT density (density obtained from the CT images by applying the calibration equation). The CT density for each of the sample deviated <5% from the measured bulk density (ρ_{wet}), indicating the effectiveness and precision of CT images in predicating bentonite bulk density. Assuming $\rho_{CT=}\rho_{wet}$, the dry density (ρ_{dry}), porosity (ϕ) and degree of saturation (S_r) of the collected bentonite samples after the experiments can then be calculated as:

$$\rho_{dry} = \frac{m_{dry}}{m_{wet}/\rho_{CT}} \qquad \text{Eq. (1)}$$

$$\phi = 1 - \frac{\rho_{dry}}{\rho_{mineral}} \qquad \text{Eq. (2)}$$

$$S_r = \frac{m_{wet}-m_{dry}}{\rho_{water}\phi m_{wet}/\rho_{CT}} \qquad \text{Eq. (3)}$$

Where m_{dry} refers to the stable sample mass measured after oven drying at 70 ºC for over 1 month, and $\rho_{mineral}$ is the mineral or grain density. ρ_{water} is water density at 1 g/cm^3.

Here 2.623 g/cm^3 was used for the mineral density of MX-80 Wyoming bentonite as measured by Karnland et al. (2006).

It is noted that oven drying under 70 ºC may underestimate the water content. Detailed quantifications on the temperature impact were conducted under 70 ºC and 130 ºC, using (1) raw bentonite (after sieving for grain size <600 μm) with 3 parallel samples; (2) two types of bentonite samples with different added water. Results showed that under 130 ºC, the measured water content of the raw bentonite material was 0.089 ± 0.0002, while the value measured under 70ºC was 0.085± 0.0003. For bentonite samples with added water and under 130 ºC, the measured water contents were 0.497± 0.0106 in 10 parallel samples and 0.199± 0.0011 in 5 parallel samples. The corresponding values measured under 70ºC were 0.491± 0.0095 and 0.196±0.0025. For the column tests conducted at water contents ranged from 0.17 (before the heating and hydration experiments) to 0.55 (after the heating hydration experiments), the water content measured under 70ºC was expected to be underestimated <1.3%. Based on these characterizations, the water content and other parameters (dry density, porosity and degree of saturation) were calibrated in the raw material and the post-mortem samples.

It is also noted the wide range of grain density reported for MX-80 Wyoming bentonite. Karnland et al. (2006) conducted systematic lab characterizations on the physical, mineralogical and chemical properties of MX-80 Wyoming bentonite. They measured the grain density using volumetric flasks in different solutions, i.e., kerosene, 1.0 and 3.0 M NaCl solutions, and 1.0 M $CaCl_2$. They did not use pycnometers or pure water because of the massive swelling of bentonite. The grain density measured with kerosene was 2.623 g/cm^3, while the values were considerably higher at 2.769, 2.777 and 2.753

g/cm^3 by using 1M $CaCl_2$, 1M NaCl and 3M NaCl solutions. They attributed the high measured grain density to the intercalation of water between the individual 2:1 montmorillonite mineral layer by polar liquid containing water, but not of kerosene. They concluded that the volume of the solid was reduced in the presence of water, which resulted in the higher grain density from the measurements. The concept of a change in grain density was supported by literature XRD data and by the major difference between surface area measured using Brunauer-Emmett-Teller (BET) analysis and theoretical specific surface area. In this study, the 2.623 g/cm^3 grain density measured by kerosene was used for calculating bentonite porosity and degree of saturation to eliminate potential water intercalation impacts on the measurement.

3. Results and discussion

In this section, the 3-D CT images and overall CT density distribution of bentonite in the non-heated control column are first presented in Section 3.1. Section 3.2 shows the temperature profile in the test column that is subject to heating and hydration. Section 3.3 describes CT density distributions during heating and hydration as calculated from 3-D CT images. In Section 3.4, the structural deformation of bentonite is discussed by tracking some local and representative tracer particles. Finally, the deformation strain from X-ray CT imaging and porosity of collected bentonite samples are compared in both columns in Section 3.5. The ERT scans and effluent water chemistry after experiments are not the focus of this study and will be reported independently.

3.1 CT density distribution from hydration

Figure 2(a) depicts the 3-D orthogonal view of CT density distribution and selected time-lapse images in the non-heated column. The color bar bounds value changes from 1.2

to 2.4 g/cm^3, with brighter yellow color indicating higher density. The sub-image at t=0 days shows the initial conditions and CT density distribution after compaction, including 1- heater and heater shaft in the center, 2- bentonite compacted between the sand layer and the central shaft, 3- the sand layer surrounding bentonite, 4- one of the ERT array emplaced at the sand-clay boundary. The CT density variations and compaction layers in bentonite and the crack (bounded by the white dotted lines in Figure 2(a)) induced by uneven compaction were expected to result in preferential flow of water in the following hydration process. Overall, the average CT density of bentonite was 1.46 g/cm^3, similar to the gravimetrically measured bulk density at 1.44 g/cm^3. The initial gravimetric water content and dry density were 0.17 and 1.20 g/cm^3, respectively (see Table 1). The porosity was then calculated as 0.53 by Eq. (2).

At t=1 day, the sand layer was saturated with water followed by a constant water injection at 0.11 mL/min while maintaining 0.83 MPa vessel pressure. Hydration was monitored by the changes of CT density, as shown at t=8 days in Figure 2(a). The figure also presents a decrease in CT density along the sand-clay boundary relative to adjacent bentonite, which might be attributed to the more pronounced dry density reduction by swelling rather than increased water content after hydration. The high-density region represents the hydration front, which by 8 days has advanced halfway to the center shaft (marked by the white arrows in the figure) from the sand layer saturated with water. Clay swelling along the sand-clay boundary may compress the interior clay, contributing to the peak density increase. At t=8 days, Figure 2(a) depicts sealing of the crack by bentonite swelling. The high-permeability crack initially provided preferential flow pathways for water intrusion into bentonite, sealing of the crack by bentonite swelling then closed these flow pathways, and hindered the hydration propagation along the crack (see the magnified image in Figure 2(a) and Figure S3 of SI). After that, the hydration is axi-symmetrical from the sand layer surrounding the compacted bentonite. At *t*=29 days, the hydration front propagates to the central shaft (Figure 2(b)), then the CT density distribution becomes more uniform as shown at 255 days in Figure 2(a) and persists until the end of the experiment at 561 days.

To quantify bentonite CT density and variations with hydration, a 2-D plane normal to the middle heater was selected (bounded by the yellow dotted box in Figure 2(a)), and the radially averaged density vs. distance from the central shaft in this plan was presented in Figure 2(b). While bentonite hydration from the sand boundary is the dominant process contributing to the spatiotemporal density distribution, Figure 2(b) also shows bentonite CT density increases ahead of the density peak (the hydration front) at the early time. For instance, at locations <25 mm away from the central shaft, bentonite CT density increases the same amount by 0.055 g/cm^3 from 2 days to 4 days, and 0.035 g/cm^3 from 4 days to 8 days. These CT density increases represented compression of interior clay by swelling at the sand-clay boundary. After the hydration front propagates to the central shaft at 29 days, Figure 2(b) also depicts a mechanical disturbance zone distributed from about 25 mm away from the central shaft to the sand-clay boundary (bounded by the two red dotted lines in the figure). Within this disturbance zone, bentonite CT density can be both higher and lower than the stable value obtained at the end of the experiment (shown by the blue curve), depending on the location and the dominant mechanical deformation/displacement behavior. Closer to the sand-clay boundary, swelling results in a CT density 0.05 g/cm^3 lower than the stable value, accompanied by a mechanical compression of interior bentonite (25-55 mm away from the heater shaft) and a CT density 0.05 g/cm^3 higher than the stable value. As hydration continues, the CT density gradient gradually diminishes and converges to the stable values as marked by the blue and red arrows in Figure 2(b). Beyond this mechanical disturbance zone and closer to the central shaft, bentonite was compressed at t=4 days, followed by monotonic density increase with hydration until the stable values. These dynamic and cm-scale variations in the mechanical behavior of bentonite buffer and evolutions of the mechanical disturbance zone (especially at the early stage of hydration) would inevitably impact the distributions of bentonite dry density, porosity and permeability, etc. In Section 3.4, the dynamic displacements of bentonite in this mechanical disturbance zone were further discussed by some tracer “particles”. More details on the time-lapse CT images, and evolution of CT density vs. radial distance from the central shaft can be seen in Figure S5 of SI.

After the experiment, the column was dismantled and bentonite samples were collected at different locations. Figure 2(c) shows the dry density and degree of saturation measured from the collected samples at the end of the experiment, as well as their variations vs. radial distance from the central shaft. The high degrees of saturation (0.9 to 1.0) represented the hydration state at the end of the experiment, resulting in the increase of CT density from 1.46 g/cm^3 to 1.68 g/cm^3 after hydration for 561 days (see Table 1). Meanwhile, the dry density varied from 1.11 to 1.16 g/cm^3, presenting higher values at 30-60 mm away from the central shaft in the mechanical disturbance zone. This non-uniform dry density distribution indicated mechanical deformation of bentonite after hydration, which will be discussed in detail in Section 3.4.

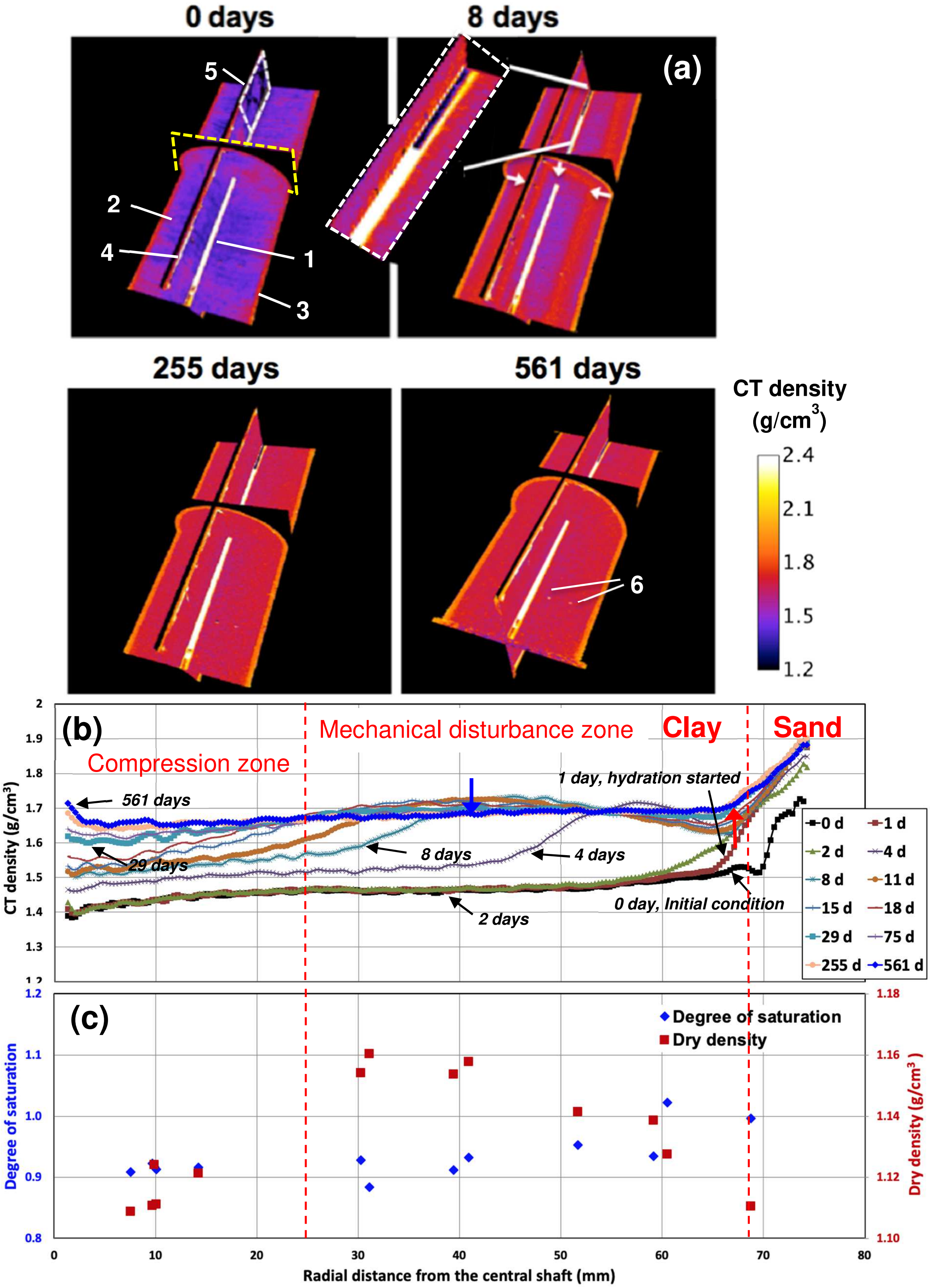
0 days
8 days
(a)
5
2
4
1
3
255 days
561 days
6
CT density (g/cm^3)
2.4
2.1
1.8
1.5
1.2
(b)
Compression zone
Mechanical disturbance zone
Clay
Sand
561 days
29 days
8 days
4 days
2 days
1 day, hydration started
0 day, Initial condition
CT density (g/cm^3)
2
1.9
1.8
1.7
1.6
1.5
1.4
1.3
1.2
0 d
1 d
2 d
4 d
8 d
11 d
15 d
18 d
29 d
75 d
255 d
561 d
(c)
Degree of saturation
Dry density
Degree of saturation
1.2
1.1
1.0
0.9
0.8
Dry density (g/cm^3)
1.18
1.16
1.14
1.12
1.10
0
10
20
30
40
50
60
70
80
Radial distance from the central shaft (mm)

Figure 2. (a) Selected time-lapse images showing the 3-D CT density distribution and variations as a function of time in the non-heated column. (b) The radially averaged CT density vs. radial distance from the central shaft in a 2-D plane. (c) The dry density and degree of saturation measured from collected bentonite samples after the experiment and their variations vs. radial distance from the central shaft. The sub-image at 0 days in (a) represents the initial condition after packing, including 1- heater and heater shaft, 2- compacted bentonite, 3- sand layer, 4- ERT arrays, 5- crack in bentonite (black color) induced by uneven compaction. The two bright spots (marked by '6') in the sub-image at 561 days represent emplaced thermocouples. The yellow dotted box in (a) at *t*=0 days bound the selected 2-D plane for plotting (b). The white arrows at *t*=8 days depict the continuous hydration from the surrounding sand layer, while the magnified image presents the preferential water intrusion along the crack at the early time. The red dashed lines in (b) bound the clay-sand boundary, the mechanical disturbance zone where bentonite compression and swelling occurred sequentially, and the compression zone where bentonite was dominated by mechanical compression. The red arrow indicates the gradual increase of CT density along the boundary after swelling and hydration, while the blue arrow represents the density decrease in the inner part of bentonite from 8 days to the end of the experiment.

3.2 Temperature profile from heating and hydration

Figure 3 presents the temporal temperature variations at different radial distances from the heater shaft, while Figure S4 in SI shows the corresponding temperature variation vs. radial distance from the heater shaft at different times. After *t*=125 days, the temperature became stable throughout the column until the end of the experiments. Note the large temperature gradient (5.6°C/mm) within 10 mm away from the heater shaft, which was 5.5 times higher than that from 10 to 20 mm away from the heater shaft. This may be attributed to the thermal conductivity changes of bentonite subject to water vaporization under 200°C. Xu et al. (2019) reported thermal conductivity of MX-80 bentonite moisturized at 0 to 22% water contents and constant dry density at 1.3 g/cm^3. Their results showed that at 90°C, the thermal conductivity of 17% water content sample could be 4 times higher than that of the dry sample. In addition, for moisturized samples, test results showed the increase of thermal conductivity as a function of temperature increase, while the dry sample presented constant thermal conductivity that was independent of temperature changes. Although data above 100°C was limited, a large thermal conductivity contrast between dry and moisturized bentonite could potentially contribute to the high thermal gradient observed near the heater shaft.

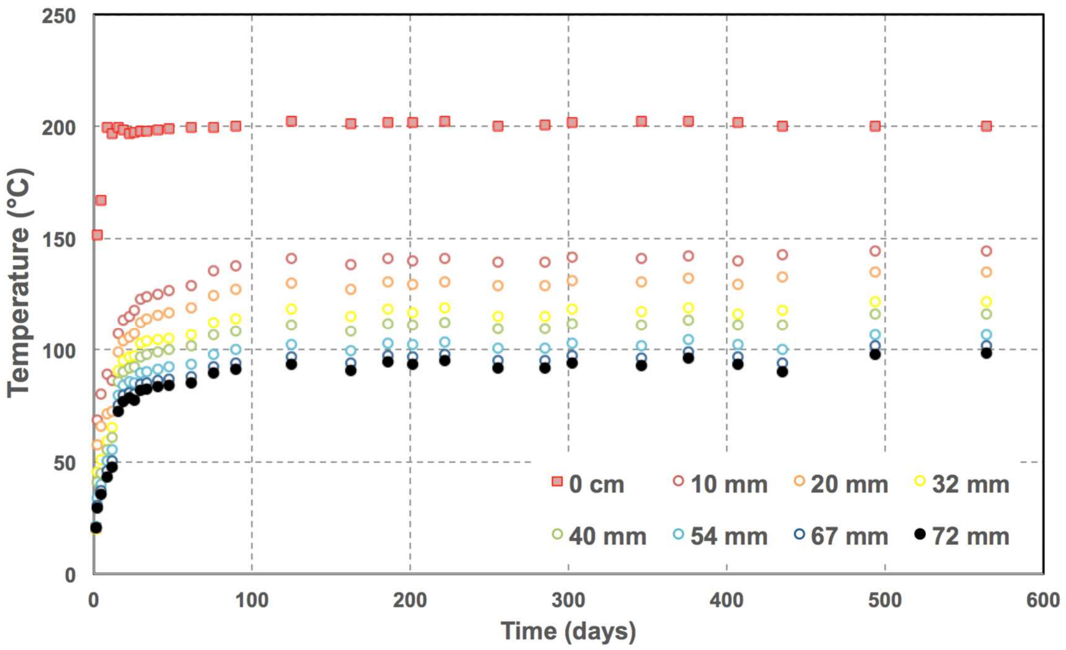

Figure 3. Temperature variations as a function of time and radial distance from the heater shaft in the heated column.

3.3 CT Density distribution from heating and hydration

Figure 4 is the 3-D CT density distribution and temporal variations in the heated column for 564 days. The bentonite was compacted to an initial CT density of 1.44 g/cm^3, close to the gravimetrically measured value at 1.41 g/cm^3. The measured gravimetric water content was 0.18, and dry density and porosity were calculated as 1.20 g/cm^3 and 0.54, respectively. Similar to the non-heated column, Figure 4 presents (1) heterogeneous structures in the compacted bentonite, including the crack and compaction layers (see Figure 4 sub-image at 0 days), (2) CT density increase by hydration from the sand boundary, and (3) swelling of clay near the clay-sand boundary and crack sealing after hydration (see Figure 4 sub-image at 8 days). At the end of the experiment (564 days), the average bentonite CT density was measured at 1.64 g/cm^3 in the heated column, lower than the value of 1.68 g/cm^3 in the non-heated column (Table 1).

Heating of the column, however, created a different CT density distribution from the non-heated control column at an early time. At *t*=8 days, Figure 4(a) shows a low-density zone around the heater shaft after heating. The average CT density in this dry-out zone was measured as 1.40 g/cm^3 at *t*=8 days, lower than the value of 1.56 g/cm^3 in the same region of the non-heated column. Figure 4(b) depicts the radially averaged CT density vs. distance from the heater shaft in a 2-D plane (bounded by the yellow dotted box in Figure 4(a)), presenting (1) larger density gradient ahead of the density peak (hydration front) than that in non-heated column, and (2) faster propagation of hydration front towards the heater shaft at 2, 4, 8 and 11 days. The larger density gradient ahead of the hydration front can be attributed to the vaporization of the initial moisture in the innermost heating zone. For example, at 2 days as heating started, CT density reduction can be observed at <20 mm away from the heater shaft in Figure 4(b). It is noted that temperature on the heater shaft was measured as 152°C during this time, lower than the water boiling temperature (172°C) at 0.83 MPa. The observed CT density reduction around the heater shaft indicates that local pressure may be lower than the applied boundary pressure in the sand layer, allowing for water evaporation to occur at the innermost heating zone. Meanwhile, hydration and swelling of bentonite at the boundary compressed the inner part of the column and resulted in the quick increase of CT density around the heater shaft from 2 days to 4 days. The condensation of water vapor in this cooler area from the inner hot zone surrounding the heater may also contribute to the quick density increase. Compared to the non-heated column, heating may result in more compression of the interior bentonite by swelling at the clay/sand boundary at early time, contributing to the faster propagation of the peak CT density in addition to the larger moisture gradient. The drier and more compressed bentonite around the heater shaft is expected to induce more pronounced swelling deformation after the hydration front arrives, which will be presented in Section 3.3.

At a later time, as the hydration front arrived 4 mm away from the heater shaft at 29 days, Figure 4(b) shows a large density drop ahead, corresponding to the dry-out zone induced by heating. At the same time, CT density became more uniform towards the end of the experiment at 564 days (marked by blue curve), after the early-stage swelling along the sand-clay boundary and mechanical compression of interior bentonite. Note that from 4-11 days, bentonite swelling along the sand-clay boundary results in a CT density 0.1

g/cm^3 lower than the final value, accompanied by compression of interior bentonite with 0.11 g/cm^3 higher than the final value. These values are twice as high as those in the non-heated column. Meanwhile, heating induced a larger mechanical disturbance zone between the dry-out zone and the sand-clay boundary, extending from 4 mm to 69 mm away from the heater shaft. By comparison, the mechanical disturbance zone in the non-heated column ranged from 25 to 68.5 mm away from the central shaft (see Figure 2(b)). By the end of the experiment (t=564 days), bentonite CT density decreased from 1.67 to 1.57 g/cm^3 from the sand boundary to the inner part of the mechanical disturbance zone, maintaining a larger density gradient than that in non-heated column from 1.69 to 1.65 g/cm^3. More details on the time-lapse CT images and the temporal evolution of CT density vs. distance from the heater shaft by heating and hydration are presented in Figure S6 of SI. Similar to the non-heated column, bentonite samples after heating and hydration presented a high degree of saturation from 0.9 to 1.0, and the radially non-uniform dry density distribution shown in Figure 4(c). At the same time, heating induced larger bentonite deformation and dry density variations in bentonite. More discussion can be seen in Sections 3.3 and 3.4.

Figure 4(a) and (b) also show a high-density layer along the heater shaft beginning to form at t=75 days in the dry-out zone. The CT density and thickness of this layer continued to grow until the end of the experiment, as illustrated by a close-view figure in Figure 4(a) at t=255 days. At t=564 days, the density stabilized at 1.90 g/cm^3 with a thickness of 3 mm. As this high-density layer became thicker, the dry-out zone expanded to a thickness of 8 mm from the heater shaft, as marked by the red dash lines in Figure 4(b). After the experiments, the column was dismantled and the high-density layer on the heater shaft was collected. XRPD analysis showed that the layer was composed entirely with anhydrite

($CaSO_4$) (see Table 2). The precipitation of pure anhydrite indicated a gap between the heating shaft surface and the bentonite was first present, providing the space for anhydrite to crystallize. This initial gap could be caused by the shrinking of bentonite after heating and drying. It could also result from the outwards displacement of bentonite as anhydrate precipitated and grew on the heater shaft. In any case, the CT image data clearly shows that this was a very localized phenomenon (coupled mechanical and chemical processes) that was initiated at the heater-bentonite interface, followed by continuous precipitation of pure anhydrite and dry-out zone expansion.

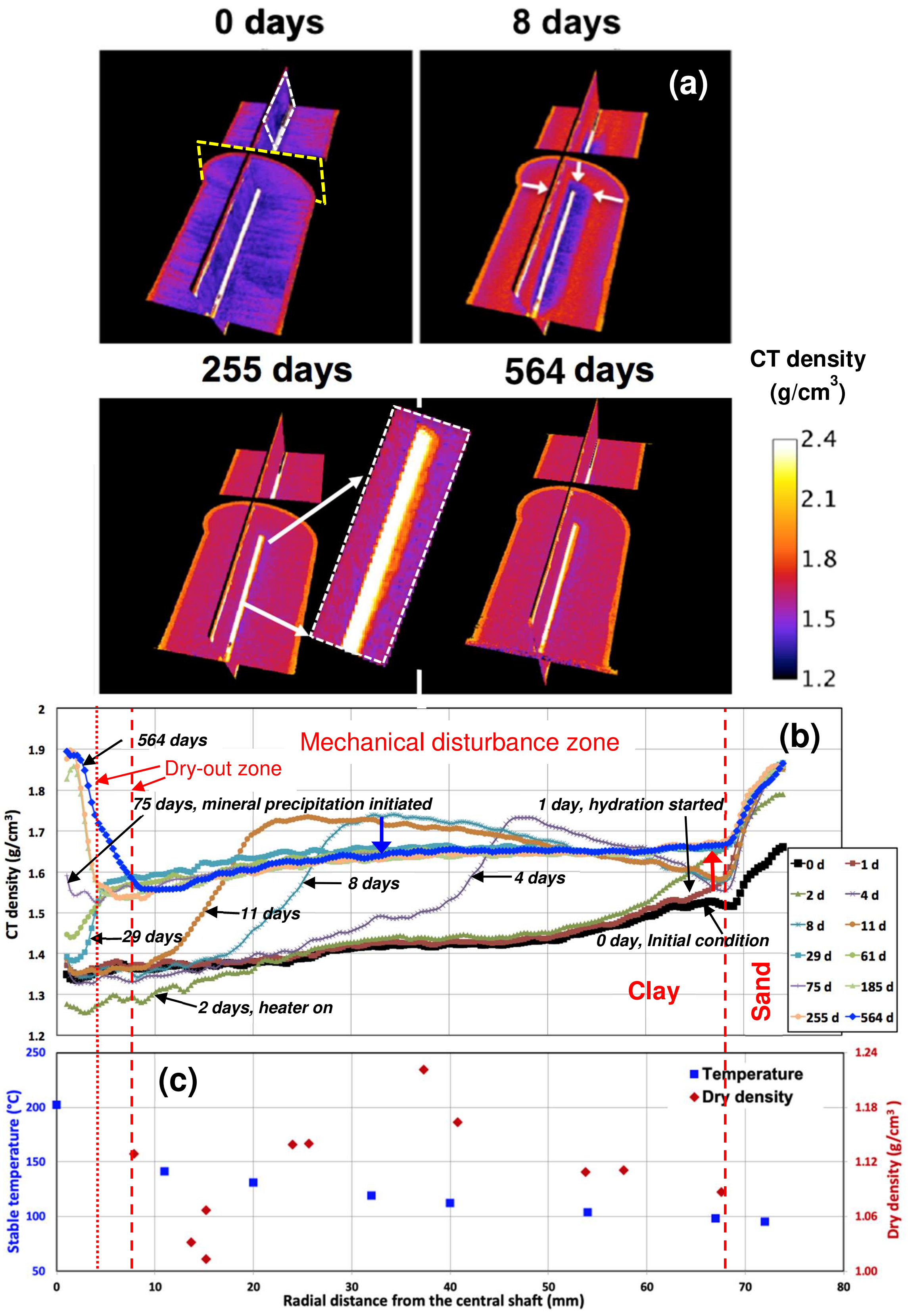
0 days
8 days
(a)
255 days
564 days
CT density (g/cm³)
2.4
2.1
1.8
1.5
1.2
(b)
Mechanical disturbance zone
564 days
Dry-out zone
75 days, mineral precipitation initiated
1 day, hydration started
8 days
4 days
11 days
29 days
0 day, Initial condition
2 days, heater on
Clay
Sand
CT density (g/cm³)
2
1.9
1.8
1.7
1.6
1.5
1.4
1.3
1.2
0 d
1 d
2 d
4 d
8 d
11 d
29 d
61 d
75 d
185 d
255 d
564 d
(c)
Temperature
Dry density
Stable temperature (°C)
250
200
150
100
50
Dry density (g/cm³)
1.24
1.18
1.12
1.06
1.00
0
10
20
30
40
50
60
70
80
Radial distance from the central shaft (mm)

Figure 4. (a) Selected time-lapse images showing the 3-D CT density distribution and variations as a function of time in the heated column. (b) The radially averaged CT density vs. radial distance from the heater shaft in a 2-D plane. (c) The variations of temperature and degree of saturation in bentonite samples as a function of radial distance from the heater shaft. The sub-image at 0 days in (a) shows the initial condition after packing, and the crack in bentonite (marked by the white dotted lines) induced by uneven compaction. The yellow dotted lines in (a) at *t*=0 days bound the selected 2-D plane for plotting (b). The white arrows at *t*=8 days depict the continuous hydration from the surrounding sand layer. The magnified image at 255 days presents the high-density layer deposited on the heater shaft. The red dashed lines in (b) bound the dry-out zone, the mechanical disturbance zone and the clay-sand boundary by the end of the experiment, while the dotted line represents the boundary of the dry-out zone from 0 to 75 days. The blue and red arrows in (b) represent the trending of bentonite CT density variations from the early time to the end of the experiment.

Table 2 also presents the mineralogical variations in the collected bentonite samples at the end of the experiments. The raw bentonite material was composed mainly by montmorillonite with 1-layer hydrate (79%), i.e., there was a single water layer per montmorillonite mineral layer. In the non-heated column, the collected bentonite samples showed the presence of gypsum and increase in plagioclase. More noticeably, montmorillonite was 2-layer hydrated (two water layers between the mineral layer) or 3-layer hydrated (three water layers between the mineral layer), with the hydration level increased towards the center of the vessel, but never reached a 100% amount of montmorillonite with 3-layer hydrates. In the samples collected from the heated vessel, all the samples contained montmorillonite with three water layers in the mineral interlayer, except for the sample closer to the heater (6.35 mm away from the heater shaft), where about 45% of the total montmorillonite amount was 2-layer hydrates, showing a loss in moisture by heating.

Table 2. Mineralogical composition (weight %) of the investigated bentonite samples, including the raw sample and samples collected from the non-heated and heated columns after the experiments.

	Heated column					**Non-heated column**			**Raw bentonite**
Sampling locations*	**<3 mm**	**6.35 mm**	**19.1 mm**	**38.1 mm**	**63.5 mm**	**19.1 mm**	**38.1 mm**	**63.5 mm**	**-**
Montmorillonite 19Å (3-layer hydrates)	0	36	64	62	63	50	13	8	0
Montmorillonite 16Å (2-layer hydrates)	0	29	0	0	0	2	37	43	0
Montmorillonite 12.5Å (1-layer hydrate)	0	0	0	0	0	0	0	0	79
Phlogopite	0	2	2	2	1	3	2	1	0
K-feldspar	0	1	2	1	1	3	3	2	1
Quartz	0	15	11	13	17	16	14	15	9
Cristobalite	0	0	2	4	4	8	6	6	4
Plagioclase	0	7	7	9	3	7	17	15	6
Calcite	0	0	0	0	0	0	3	3	1
Halite	0	0	0	0	0	0	0	0	0
Pyrite	0	1	1	1	0	1	0	1	0
Anhydrite	100	0	0	0	0	0	0	0	0
Gypsum	0	9	12	8	11	10	4	7	0

Note: *The numbers under each column represent the radial distance from the central/heater shaft. Axially, all bentonite samples after column tests were collected at 9-12 cm from the end cap.

3.4 Displacement

In this section, the mechanical behavior of bentonite subject to hydration and heating was further quantified by tracking the displacements of thermocouple sensors (working as tracer “particles”) emplaced in both columns and imaged through frequent X-ray CT scans.

3.4.1 Dynamic displacement from hydration

Figure 5(a) depicts the 2-D CT images selected from the non-heated column at different times, while Figure 5(b) is the magnified image focusing on the displacement of the tracer particle. The tip of the white arrow in Figure 5(a) and crossing of the dotted lines in Figure 5(b) point to the initial location of the tracer particle before hydration, i.e., 48 mm away from the central shaft. The sub-image at *t*=0 days in Figure 5(a) presents the compacted bentonite, the surrounding sand layer, the brightly white shaft and inserted heater (never turned on during the experiment) in the center, and the cross-section of the ERT arrays emplaced at the sand-clay boundary. The sub-images at *t*=4 and 8 days in Figure 5(a) depict that as the hydration front (marked by the white dotted circle) propagated from the surrounding sand layer to interior bentonite, swelling along the sand-clay boundary induced considerable density reduction. Meanwhile, the tracer particle was pushed towards the central shaft along with the compression of surrounding clay (see the offset of the particle relative to the arrow tip in Figure 5(a) and the dotted lines crossing in Figure 5(b)). At *t*=8 days, the offset was maximum as hydration front passed the tracer particle, followed by reverse displacement to its original location.

The distance between the particle and the central shaft was measured and normalized to 0 before the experiment. Figure 5(c) presents the dynamic displacement vs. time in red curve, in which a negative displacement is defined when the particle moves towards the central shaft, whereas a positive displacement is defined when the particle moves outward from its initial position. Also plotted with the blue curve in the figure is the bentonite CT density around the tracer particle. At early time (1-8 days), the displacement continuously decreased from 0 mm to the lowest value of -2.3 mm, representing that the inner part of bentonite was dominated by compression as the hydration boundary of bentonite was dominated by swelling. After the inner part of bentonite was gradually hydrated, the displacement rebounded back because of the swelling of bentonite in the column interior. This might also result in the gradual decrease of bentonite CT density after 8 days shown in Figure 5(c). By the end of the experiment (561 days), the displacement and bentonite CT density were relatively stable at -0.77 mm and 1.68 g/cm^3, respectively.

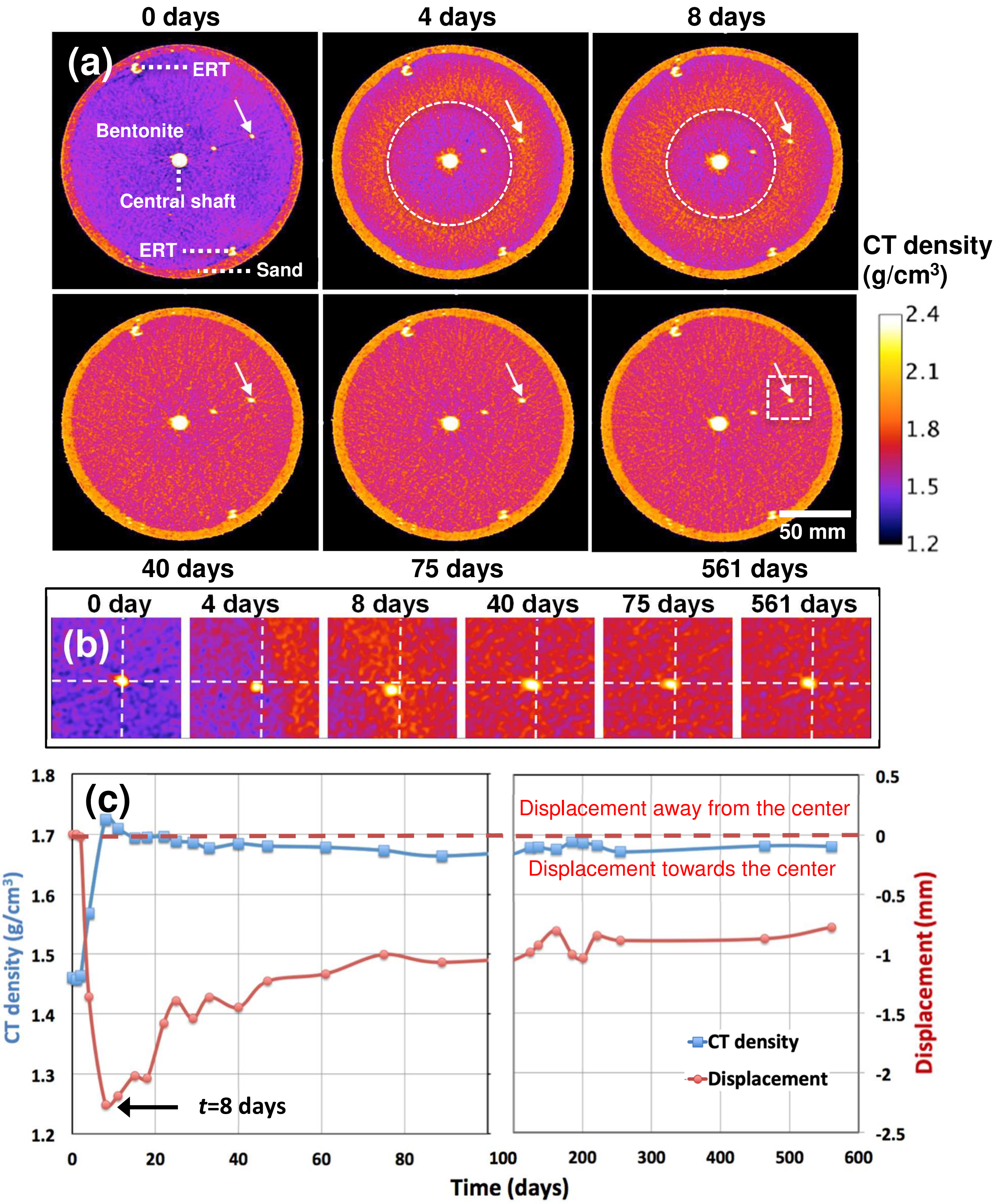

Figure 5. (a) Selected time-lapse 2-D CT images showing the displacement of the selected tracer particle and temporal CT density distributions in the non-heated column. (b) The magnified images showing the displacement of the tracer particle relative to its initial

location marked by the crossing of the white dotted lines. (c) Dynamic displacement of the tracer particle and surrounding bentonite CT density variations as a function of time. The white dotted circles in (a) mark the high-density hydration front and the white arrows point to the initial position of the tracer particle before test. The white dotted box in (a) at 561 days bounds the magnified images in (b).

3.4.2 Dynamic displacement from heating and hydration

Figures 6(a) and (b) are the 2-D time-lapse CT images and displacement of the tracer particle located 11 mm away from the central shaft in the heated and hydrated column. In addition to the heater, central shaft and ERT arrays in Figure 5(a), Figure 6(a) also presents electrical wires connected to the thermocouple sensors (see the sub-image at 0 days of Figure 6(a)). Similar to the non-heated column, the inward displacement of the tracer particle at early time (1-8 days) was followed by the outward displacement to its original location at *t*=22 days (see the red curve in Figure 6(c)). Different from the non-heated column, however, the particle continued to move away from the central shaft until the end of the experiment at t=564 days (see the magnified image in Figure 6(b)). In Figure 6(c), as heating started at *t*=2 days, bentonite CT density surrounding the tracer particle sharply reduced due to water vaporization, followed by a quick rebound at *t*=4 days due to compression by swelling along the sand-clay boundary. At *t*=8 days, displacement was minimum at -1.1 mm towards the heater shaft. After the hydration front arrived, the drier and more comp bentonite swelled more pronouncedly than the non-heated bentonite, inducing more outward displacement of the tracer particle at 40, 75 and 564 days in Figure 6(a) and (c). At the end of the experiment, the displacement and bentonite CT density were measured as 1.25 mm and 1.59 g/cm^3, respectively.

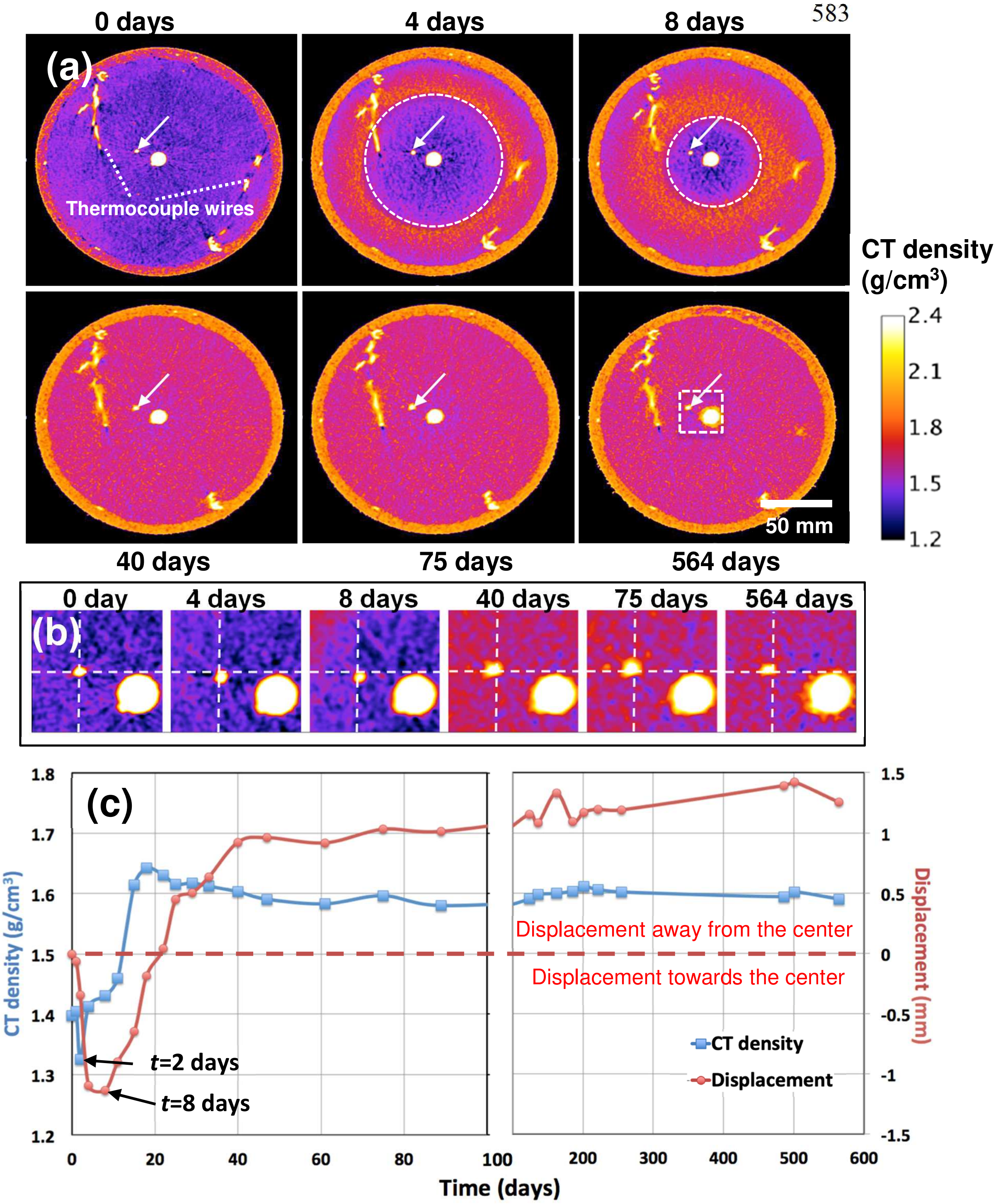

Figure 6. (a) Selected time-lapse 2-D CT images showing the displacement of the selected tracer particle and temporal CT density distributions in the heated column. (b) The magnified images presenting the displacement of the tracer particle relative to its initial

location marked by the crossings of the white dotted lines. (c) Dynamic displacement of the tracer particle and surrounding bentonite CT density variations as a function of time. The white dotted circles in (a) mark the high-density hydration front and the white arrows point to the initial position of the tracer particle before test. The white dotted box in (a) at 564 days bounds the magnified images in (b).

3.4.3 Spatiotemporal displacement

The spatiotemporal displacement of bentonite was further analyzed by tracking the six radially distributed thermocouples (working as tracer "particles"). Figures 7(a) and (c) show the radial distribution of each thermocouple in the non-heated (a) and heated (c) columns, while Figures 7(b) and (d) depict observed displacements and variations for 1.5 years. In both columns, particle '*a*' is closest to the central shaft, while *f* is closest to the sand-clay boundary, exact locations are noted in the Figures 7(b) and (d). In the non-heated column, as shown in Figure 7(b), all six particles behave similarly. At early time (1-8 days), all particles moved with the surrounding clay and were displaced inward towards the central shaft. After that, as hydration propagated to the center, all the tracer particles were pushed outward towards their initial positions. By the end of the experiment at t=561 days, the displacements ranged from -0.4 to -0.8 mm.

Compared to the non-heated column, larger displacements occurred when subject to heating and hydration. As shown in Figure 7(c) and (d)), at early time (1-8 days), the displacements range from -1.0 to -3.8 mm, showing larger compression deformation than that in the non-heated column (-0.2 to -2.4 mm). At later time (11 to 564 days), all the tracer particles moved outward. By the end of the experiment, the displacement varied from -0.82 (towards the heater shaft) to 1.25 mm (away from the heater shaft), resulting in larger shifts than those observed in the non-heated column shown in Figure 7(b).

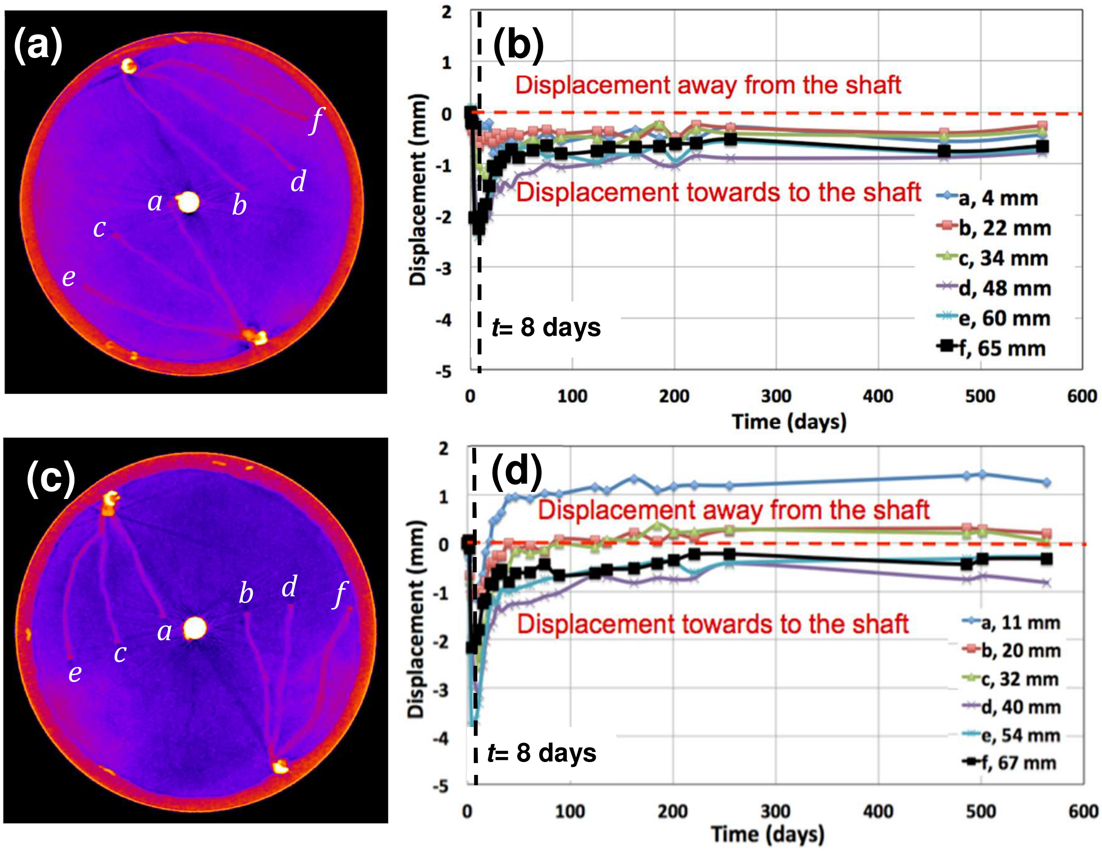

Figure 7. The six tracer particles that were used for tracking bentonite displacement at different locations in the non-heated (a) and heated (c) columns. Panels (b) and (d) show the displacements as a function of time. The numbers in the legends of (b) and (d) are the

initial positions of each tracer particle relative to the central shaft. The vertical black dotted lines in (b) and (d) mark the minimum displacement at *t*=8 days.

3.5 Comparison of strain with porosity in the mechanical disturbance zone

Comprehensive CT imaging data showed closely coupled mechanical evolution of the bentonite buffer with simultaneous heating and hydration. Figure 8 further compares the strain changes vs. radial distance from the central shaft in both columns, at early time (8 days) and at the end of the experiments. Assuming radially symmetrical deformation of bentonite induced by heating and hydration, the strain (ε) was calculated from displacement (ΔL) of the tracer particles shown in Figure 7 and the column radius (R), i.e., $\varepsilon = \Delta L/R$. Also shown in the figure are porosity distributions measured from bentonite samples after dismantling of both columns. Note the heater was 30 cm long. The tracer particles were emplaced at the same axial level (11 cm from the middle heater) in both columns, and bentonite samples were collected at the end of the experiment in the plane normal to the middle heater. Thus the strain and porosity shown in Figure 8 are representative of the axial segment most impacted by heating and hydration. The blue and red curves in the figure are initial porosity distribution of the plane normal to the middle heater calculated from CT images as:

$$\phi_i = 1 - \frac{(1-w)\rho_{CT}}{\rho_{mineral}} \qquad \text{Eq. (4)}$$

Where w refers to the initial water content, 0.17 for the non-heated column and 0.18 for the heated column.

As shown in Figure 8(a), at early time (8 days), strain in the non-heated column increased from -0.035 at 60 mm to 0 at 4 mm away from the central shaft. Closer to the clay-sand boundary, e.g., 65 mm away from the central shaft, strain was slightly larger at -0.030. By the end of the experiment (561 days), strain values stabilized and varied from -0.010 to -0.006. The porosity at this time ranged from 0.55 to 0.57, higher than the initial values shown by the blue curve. The slightly negative strain and increased porosity represent sequentially occurring compression and swelling. Compression of the inner part of the column caused by swelling at the boundary was dominant at the early time of hydration. This was followed by swelling and porosity increases as hydration propagated to the center by the end of the experiment. The CT density changes before and after the experiments showed high density rings in the sand layer and along the sand-clay interface at 1.0 to 1.5 mm wide for the non-heated and 1.04 to 1.26 mm wide for the heated column. This indicates the loosely compacted sand layer surrounding the bentonite may provide space for bentonite swelling, volume expansion and porosity increase (see more details in Figure S7 of SI).

Figure 8(b) shows the spatial variations of strain and porosity in the heated column. As discussed earlier, heating induced drier and denser bentonite near the heater shaft at early time. As hydration propagated to the column center, more pronounced clay swelling near the shaft resulted in larger outward strain and higher porosity at the end of the experiment (see the green squares in Figure 8(b)). Bentonite swelling near the heater shaft and along the clay-sand boundary collectively compressed the area in between, resulting in a radially heterogeneous distribution of bentonite. These highly localized and dynamic deformations/displacements of bentonite will inevitably result in the spatial variations in its hydrological (e.g., permeability) and mechanical (e.g., swelling) properties. Detailed evaluations of these properties (e.g., Zhu et al., 2013), with modified modeling studies, will help to predict the long-term performance of bentonite buffer and the design of repositories for high-level radioactive waste.

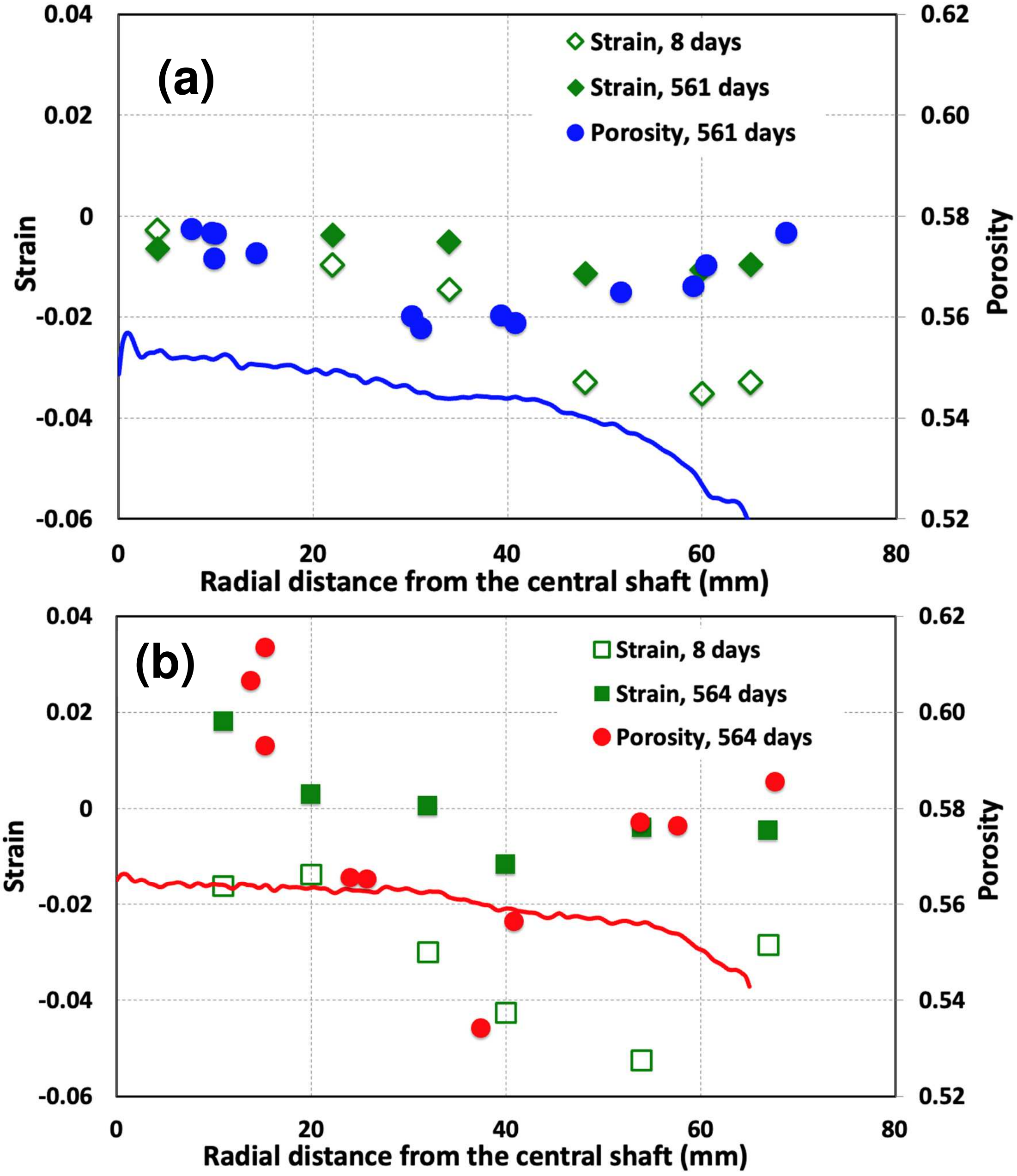

Figure 8. Comparison of strain and porosity variations as a function of radial distance from the central shaft in the non-heated (a) and heated (b) columns at early time and by the end

of the experiments. The blue and red curves represent the initial porosity distributions of bentonite surrounding the tracer particles.

More detailed characterizations on the bentonite samples after dismantling are presented in Figure 9, including water content, dry density, porosity and degree of saturation. Samples were collected axially from 7.5 to 20 cm in the non-heated column and 3.6 to 23 cm in the heated column. In the non-heated column, results presented an overall decrease of bentonite water content, porosity and degree of saturation from the hydration boundary to the central shaft. Clay swelling along the hydration boundary induced lower dry density than those closer to the central shaft. Porosities at locations <20 mm away from the heater shaft were slightly higher, consistent with the bentonite deformation and strain shown in Figure 8(a). In the heated column, Figure 9(b) shows more variations of all parameters at locations <20 mm away from the heater shaft, representing the compression area at about 40 mm away from the heater shaft, and more pronounced swelling of bentonite at the inner part of the column. At the axial direction, the middle hottest portion of the column (e.g., 21 and 23 cm away from the end cap) induced the most considerable variations in dry density and porosity, representing the spatial heterogeneity in bentonite induced by heating and hydration.

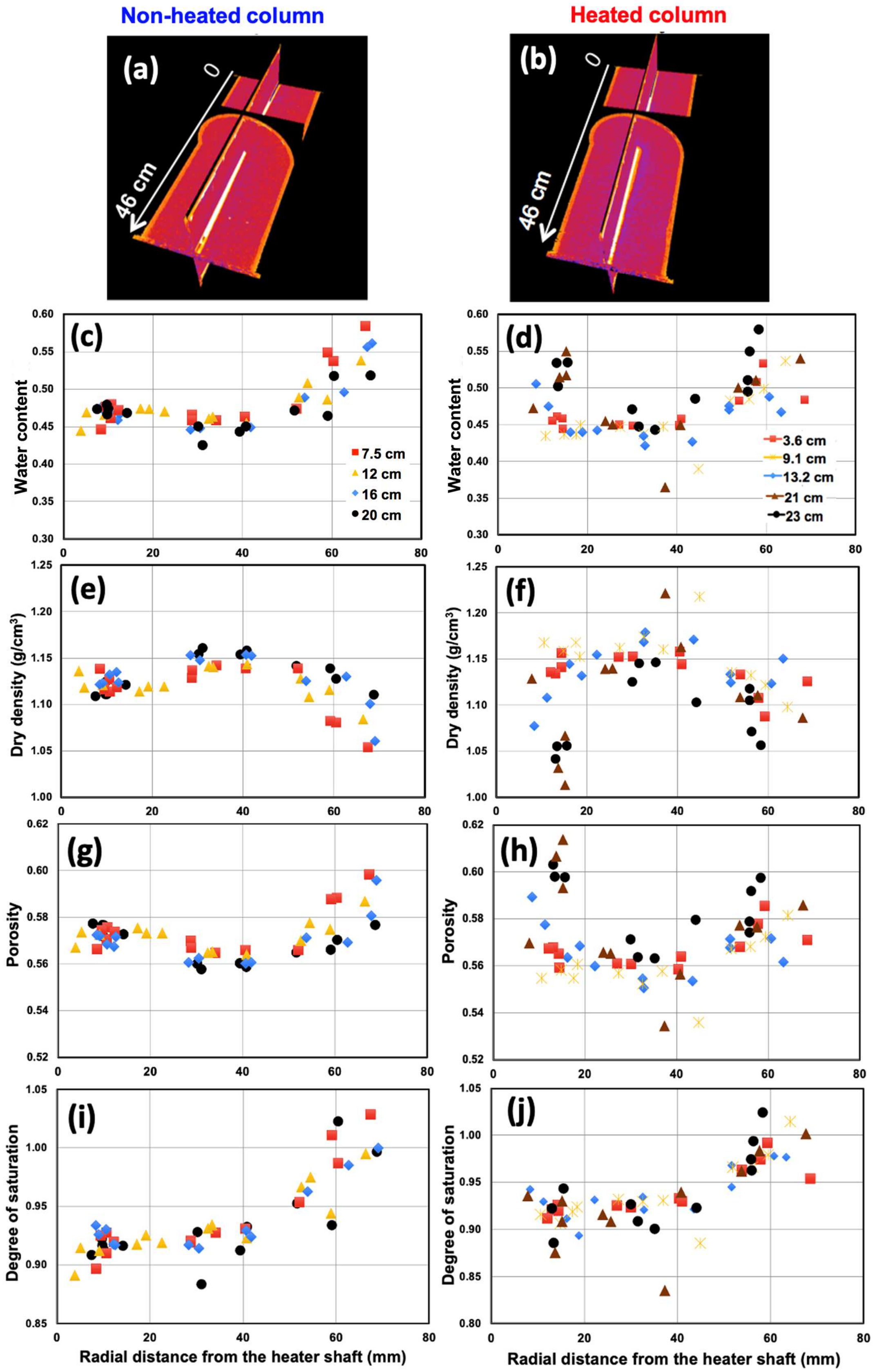
Non-heated column
Heated column
(a)
0
46 cm
(b)
0
46 cm
(c)
Water content
0.60
0.55
0.50
0.45
0.40
0.35
0.30
0
20
40
60
80
7.5 cm
12 cm
16 cm
20 cm
(d)
Water content
3.6 cm
9.1 cm
13.2 cm
21 cm
23 cm
(e)
Dry density (g/cm³)
1.25
1.20
1.15
1.10
1.05
1.00
(f)
Dry density (g/cm³)
(g)
Porosity
0.62
0.60
0.58
0.56
0.54
0.52
(h)
Porosity
(i)
Degree of saturation
1.05
1.00
0.95
0.90
0.85
(j)
Degree of saturation
0.80
Radial distance from the heater shaft (mm)
Radial distance from the heater shaft (mm)

Figure 9. Characterization of bentonite samples after the experiments and their variations as a function of radial distance from the heater shaft in the non-heated (c, e, g, i) and heated columns (d, f, h, j). The color and number in the legends of (c) to (j) represent samples collected at different axial locations in (a) and (b), with a smaller number near the end of the column and a larger number near the column center.

4. Conclusions and implications

Motivated by expanding data and knowledge base for bentonite buffers under elevated temperatures for geologic disposal of high-level radioactive waste, a bench-scale laboratory experiment on MX-80 Wyoming bentonite was conducted for 1.5 years. A radial temperature distribution was created from 200 ºC in the center to 95 ºC at the periphery. Two test columns were used, a control column undergoing only hydration, and an experimental column experiencing both heating and hydration. During the experiment, frequent X-ray CT images provided insights into the hydrological and mechanical behavior of the bentonite buffer. A detailed investigation was carried out through (1) 3-D mapping of the temporal variations in CT density distribution in both columns, (2) post-dismantling characterization of bentonite samples, and (3) evaluation of tracer particle displacements in the mechanical disturbance zone and their correlations with bentonite CT density and porosity. Along with the control tests in the non-heated column, CT imaging clearly showed a similar hydration front moving radially inward. Mechanically, bentonite swelling was observed at the clay-sand interface upon hydration, causing compression of interior bentonite, and closed fast flow paths created from column packing. After the arrival of the hydration front (e.g., at later times), the bentonite moved back toward its initial location as hydration propagated to the center. Differing from the non-heated column, however, heating induced a larger compression of inner bentonite, followed by larger and sustained swelling near the heater shaft. All these mechanical changes were closely coupled with thermal alteration, moisture migration and evaporation, and mineral precipitation in the dry-out zone.

The sealing of fast flow paths (due to initial packing heterogeneity) in both columns suggest that it is unlikely that the buffer will have fast paths for radionuclide transport once the bentonite is close to fully hydrated. The larger density variations in the heated column indicate a more complex and heterogeneous mechanical behavior of the bentonite buffer as it is subjected to heating and hydration with strong thermal and moisture gradients. These considerable variations in density and porosity (and consequently permeability) will be important in determining the feasibility of bentonite as a buffer material for high-temperature radioactive waste disposal. In addition, mineral precipitation was observed at the canister surface in the heated column experiment. Further studies are warranted whether such precipitation could affect the integrity of waste canisters in the long run. Future work will complement the experimental observations with THMC modeling studies to test our predictive capabilities and eventually conduct simulations to predict the long-term performance of bentonite buffers in radioactive waste repositories.

Conflicts of interest

The authors declare no competing financial interest.

Acknowledgements

This material was based upon the work supported by the Spent Fuel and Waste Science and Technology, Office of Nuclear Energy, of the U.S. Department of Energy under Contract Number DE-AC02-05CH11231 with Lawrence Berkeley National Laboratory. We appreciate the valuable comments provided by the reviewers and editor, which helped improve presentation of this work.

References

Åkesson, M., Jacinto, A.C., Gatabin, C., Sanchez, M., Ledesma, A., 2009. Bentonite THM behaviour at high temperatures: experimental and numerical analysis. Géotechnique 59 (4), 307–318.

Alonso, E., Ledesma, A. (Eds.), 2005. Advances in Understanding Engineered Clay Barriers. A. Balkema Pub., Leiden, p. 83.

Ballarini, E., Graupner, B., Bauer, S., 2017. Thermal–hydraulic–mechanical behavior of bentonite and sand-bentonite materials as seal for a nuclear waste repository: Numerical simulation of column experiments. Appl. Clay Sci. 135, 289–299.

Birkholzer, J. T., Bond, A. E., Hudson, J. A., Jing, L., Tsang, C. F., Shao, H., Kolditz, O., 2018. DECOVALEX-2015: an international collaboration for advancing the understanding and modeling of coupled thermo-hydro-mechanical-chemical (THMC) processes in geological systems. Environ. Earth Sci. 77:539.

Bossart, P., Jaeggi, D., Nussbaum, C., 2017**.** Experiments on thermo-hydro-mechanical behaviour of Opalinus Clay at Mont Terri rock laboratory, Switzerland. J. Rock Mech. Geotech. Eng. 9 (3), 502–510.

Börgesson, L., Chijimatsu, M., Nguyen, T.S., Rutqvist, J., Jing, L., 2001. Thermo-hydromechanical characterization of a bentonite-based buffer material by laboratory tests and numerical back analyses. Int. J. Rock Mech. Min. Sci. 38, 105–127.

Bourg, I.C., Bourg, A.C.M, Sposito. G., 2003. Modeling diffusion and adsorption in compacted bentonite: a critical review. J. Contam. Hydrol. 61 (1–4), 293–302.

Bradbury, M.H. and B., Baeyens. 2003. Porewater chemistry in compacted re-saturated MX-80 bentonite. J. Contam. Hydrol. 61 (1), 329–338.

Cheshire, M.C., Caporuscio, F.A., Rearick, M.S., Jove-Colon, C., McCarney, M.K., 2014. Bentonite evolution at elevated pressures and temperatures: An experimental study for generic nuclear repository designs. Am. Mineral. 99 (8–9), 1662–1675.

Cheshire, M.C., Caporuscio, F.A., Jove-Colon, C., Norskog, K., 2018. Fe-Saponite Growth on Low-Carbon and Stainless Steel in Hydrothermal-Bentonite Experiments. *J. Nucl. Mater.* 511, 353-366.

ENRESA, 2006. FEBEX: Updated Final Report. ENRESA Tech. Publ. PT 05-0/2006, 589 pp.

Fernández A.M., Villar, M.V., 2010. Geochemical behaviour of a bentonite barrier inthe laboratory after up to 8 years of heating and hydration. Appl. Geochem. 25 (6), 809–824.

Gómez-Espina R. and Villar M.V., 2010. Geochemical and mineralogical changes in compacted MX-80 bentonite submitted to heat and water gradients. Appl. Clay Sci. 47 (3–4), 400–408.

Harjupatana, T., Alaraudanjoki, J., Kataja, M., 2015. X-ray tomographic method for measuring three-dimensional deformation and water content distribution in swelling clays. Appl. Clay Sci. 114, 386–394.

Harjupatana, T., Miettinen, A., Kataja, M., 2022. A method for measuring wetting and swelling of bentonite using X-ray imaging. Appl. Clay Sci. 221, 106485.

Hicks, T.W., White, M.J., Hooker, P.J., 2009. Role of Bentonite in Determination of Thermal Limits on Geological Disposal Facility Design. Report 0883-1 (v 2.0) for Nuclear Decommissioning Authority. Galsons Sciences Ltd., Harwell.

Karnland, O., Olsson, S, Nilsson, U., 2006. Mineralogy and sealing properties of various bentonites and smectite-rich clay materials. Clay Technology AB, Technical Report TR-06-30.

Karnland, O., Olsson, S., Dueck, A., Birgersson, M., Nilsson, U., Hernan-Hakansson, T., 2009. Long term test of buffer material at the Äspö Hard Rock Laboratory, LOT project. Final report on the A2 test parcel. SKB report TR-09-29.

Lutterotti, L., 2010. Total pattern fitting for the combined size-strain–stress-texture determination in thin film diffraction. Nucl. Instrum. Methods Phys. Res. B 268 (3-4), 334–340.

Meunier A., Velde, B., Griffault. L., 1998. The reactivity of bentonites, a review. An application to clay barrier stability for nuclear waste storage. Clay Miner. 33, 187–196.

Mull, R. T., 1984. Mass estimates by computed tomography: Physical density from CT numbers. AJR 143, 1101–1104.

Peters, E. J., Hardham, W. D., 1990. Visualization of fluid displacements in porous media using computed tomography imaging. J. Pet. Sci. Eng. 4, 155-168.

Pini, R., Madonna, C., 2016. Moving across scales: a quantitative assessment of X-ray CT to measure the porosity of rocks. J. Porous Mater 23, 325–338.

Pusch, R., Kasbohm, J., Thao H.T.M., 2010. Chemical stability of montmorillonite buffer clay under repository-like conditions—a synthesis of relevant experimental data. Appl. Clay Sci. 47 (1–2), 113-119.

Rasband, W.S. ImageJ, U. S. National Institutes of Health, Bethesda, Maryland, USA, https://imagej.nih.gov/ij/, 1997-2022.

Rawat, A., Baille, W., Tripathy, S., 2019. Swelling behavior of compacted bentonite-sand mixture during water infiltration. Eng. Geol. 257, 105141.

Rutqvist, J., Zheng, L., Chen, F., Liu, H.H., Birkholzer. J., 2014. Modeling of coupled thermo-hydro-mechanical processes with links to geochemistry associated with bentonite-backfilled repository tunnels in clay formations. Rock Mech. Rock Eng. 47, 167–186.

Sellin, P., Leupin, O.X., 2013. The use of clay as an engineered barrier in radioactive waste management—a review. Clay Miner. 61 (6), 477–498.

Villar, M. V. and Lloret. A., 2004. Influence of temperature on the hydromechanical behaviour of a compacted bentonite. App. Clay Sci. 26, 337–350.

Villar, M.V., 2005. MX-80 Bentonite. Thermo-Hydro-Mechanical Characterization Performed at CIEMAT in the Context of the Prototype Project. Technical Report 1053. Spain, CIEMAT.

Villar, M.V., Martín, P.L., Gómez-Espina, R., Romero, F.J., Barcala, J.M., 2012. THM cells for the HE-E test: setup and first results. PEBS report D2.2.7a. CIEMAT Technical Report CIEMAT/DMA/2G210/02/2012 (Madrid, 34 pp.).

Villar, M.V., Martín, P.L., Romero, F.J., 2014. Long-term THM tests reports: THM cells for the HE-E test: update of results until February 2014. Deliverable-N°: D2.2-7.3. CIEMAT Technical Report IEMAT/DMA/2G210/03/2014.

Villar, M.V., Iglesias, R.J., Gutiérrez-Álvarez, C., Carbonell, B., 2018. Hydraulic and mechanical properties of compacted bentonite after 18 years in barrier conditions. Appl. Clay Sci. 160, 49–57.

Villar, M.V., Iglesias, R.J., García-Siñeriz, J.L., Lloret, A., Huertas, F., 2020. Physical evolution of a bentonite buffer during 18 years of heating and hydration. Eng. Geol. 264, 105408.

Villar, M.V., Gutiérrez-Álvarez, Martín, P. L., 2020. Low-suction water retention capacity of bentonite at high temperature. E3S Web of Conferences 195, 04010.

Vomvoris, S., Birkholzer, J.T., Zheng, L., Gays, I., Blechschmidt, I., 2015. THMC behavior of clay-based barriers under high temperature–from laboratory to URL scale, Proceedings, International High-Level Radioactive Waste Management Conference, Charleston, NC, USA.

Wellington, S. L., Vinegar, H. J., 1987. X-ray computerized tomography, J. Pet. Technol. 39 (8), 885–898.

Xu, T., Senger, R., Finsterle, S., 2008. Corrosion-induced gas generation in a nuclear waste repository: reactive geochemistry and multiphase flow effects. Appl. Geochem. 23, 3423–3433.

Xu, Y., Sun, D., Zeng, Z., Lv, H., 2019. Temperature dependence of apparent thermal conductivity of compacted bentonites as buffer material for high-level radioactive waste repository. Appl. Clay Sci., 174, 10-14.

Zheng, L., Samper, J., Montenegro, L., Fernández. A.M., 2010. A coupled THMC model of a heating and hydration laboratory experiment in unsaturated compacted FEBEX bentonite. J. Hydrology 386 (1–4): 80–94.

Zheng, L., Rutqvist, J., Birkholzer, J.T., Liu. H.H., 2015. On the impact of temperatures up to 200 °C in clay repositories with bentonite engineer barrier systems: A study with coupled thermal, hydrological, chemical, and mechanical modeling. Eng. Geol. 197, 278–295.

Zheng, L., Rutqvist, J., Birkholzer, J.T., Liu. H.H., 2017. Coupled THMC models for bentonite in an argillite repository for nuclear waste: illitization and its effect on swelling stress under high temperature. Eng. Geol. 230, 118–129.

Zheng, L., Xu, H., Rutqvist, J., Reagan, M., Birkholzer, J. T., Villar, M. V., Fernández, A. M., 2020. The hydration of bentonite buffer material revealed by modeling analysis of a long-term in situ test. App. Clay Sci. 185, 105360.

Zheng, L., Xu H., Rutqvuist, J. Birkholzer J.T., 2021. Coupled THMC models for bentonite barrier in nuclear waste repositories: modeling approach, validation by field test and exploratory models. ARMA 21–1340, presented at the 55th US Rock Mechanics/Geomechanics Symposium held in Houston, Texas, USA, 20-23 June 2021.

Zhu, C., Ye, W., Chen, Y., Chen, B., Cui, Y., 2013. Influence of salt solutions on the swelling pressure and hydraulic conductivity of compacted GMZ01 bentonite. Eng. Geol., 166, Pages 74-80.